

# Nonspherical modes nondegeneracy of a tethered bubble

Maxime Fauconnier,<sup>\*</sup> Jean-Christophe Béra,<sup>†</sup> and Claude Inserra<sup>‡</sup>  
 LabTAU, INSERM, Centre Léon Bérard, Université Lyon, F-69003 Lyon, France



(Received 28 April 2020; accepted 20 August 2020; published 14 September 2020)

When excited at sufficiently high acoustic pressures, a wall-attached bubble may exhibit asymmetric nonspherical modes. These vibration modes can be decomposed over the set of spherical harmonics  $Y_{nm}(\theta, \phi)$  for a degree  $n$  and order  $m$ . We experimentally capture the time-resolved dynamics of asymmetric bubble oscillations in a top-view configuration. A spatiotemporal modal analysis is performed and allowed recovering the set of zonal ( $m = 0$ ), tesseral ( $0 < m < n$ ), and sectoral ( $m = n$ ) spherical harmonics that develop at the bubble interface. The analysis of the surface instability thresholds reveals that the frequencies of asymmetric modes differ from the standard Lamb spectrum. In addition, the nondegeneracy of asymmetric modes for a given degree  $n$  is evidenced by noncompletely overlapping resonance bands. Finally, the coexistence between zonal and sectoral modes is analyzed through their modal interaction, amplitude interplay and relation of phase, as well as their geometric compatibility.

DOI: [10.1103/PhysRevE.102.033108](https://doi.org/10.1103/PhysRevE.102.033108)

## I. INTRODUCTION

A volume of gas trapped in a fluid is exposed to mechanical stresses at the liquid-gas interface, due to unbalanced inward forces. This so-called surface tension constrains the gas to minimize its interface area, forcing it to adopt the shape of a spherical bubble. In a surrounding low-pressure ultrasound field, this bubble will oscillate radially. Above a critical pressure value, instabilities develop on the bubble interface that will exhibit nonspherical deformations. It is worth mentioning that their triggering and the pressure thresholds may shift in certain circumstances since they are very sensitive to any asymmetry, which may be induced by an anisotropy in the surrounding acoustic field [1,2]. This does not work for a monochromatic low-frequency excitation, where the acoustic wavelength is much greater than the bubble's size and the surrounding field is then locally uniform. The presence of a nearby wall is another way to break the symmetry and to favor nonspherical bubble modes [3]. Such interface deformations, vectors of high mechanical energy, are widely studied and exploited in the context of therapeutic applications of ultrasound, such as localized drug delivery or transfection [4,5], lithotripsy, or blood-brain barrier opening [6].

The most common approach for investigating the shape perturbation of an initially spherical bubble is to describe its interface  $r(\theta, \phi, t)$  by the equation

$$S(\theta, \phi, t) = r(\theta, \phi, t) - R_0 - \sum_{n,m} a_{nm}(t)Y_{nm}(\theta, \phi) = 0, \quad (1)$$

where  $\theta$  and  $\phi$  are spherical coordinates,  $R_0$  is the bubble equilibrium radius,  $a_{nm}(t)$  are the time-varying amplitudes of the surface modes (including the purely radial one for

$n = m = 0$ ), and  $Y_{nm}$  are the spherical harmonics of degree  $n$  and order  $m$ . For an arbitrary nonzero  $n$ , spherical harmonics are called zonal when  $m = 0$ , sectoral when  $m = n$ , or tesseral when  $m \neq n$ . Considering an incompressible, inviscid, unbounded fluid, Lamb [7] derived the spectrum of natural angular frequencies for the shape modes

$$\omega_n^2 = (n-1)(n+1)(n+2)\sigma/\rho R_0^3, \quad (2)$$

where  $\sigma$  is the surface tension and  $\rho$  is the density of the liquid. A further analysis of the nonspherical oscillations has been performed by Plesset [8], who derived the equations of shape oscillations for small amplitudes of deformations  $|a_{nm}(t)/R_0| \ll 1$ ,  $n \neq 0$ . In this approximation the equations for both spherical and nonspherical oscillations are uncoupled. The former is the Rayleigh-Plesset equation ruling the evolution of the radial oscillation, while the latter can be reduced to the Mathieu equation describing the parametric excitation of shape modes [9]. An important feature of the equations ruling the nonspherical oscillations is that they do not contain the index  $m$ . This means that, for a given spherical harmonic of degree  $n$ , all associated order- $m$  functions are described by the same expression given by Eq. (2) and would have thus the same resonance frequency (which is referred in literature as degeneracy of spherical harmonics). By conducting a perturbation analysis, Francescutto and Nabergoj [10,11] obtained the pressure thresholds for the nonspherical oscillations that are also independent of the index  $m$  of the spherical harmonics. From this analysis, for a given value  $n$ , the set of degree- $n$  spherical harmonic modes for different orders  $m$  appears as degenerate modes. The mathematical analysis of an initially spherical bubble in an unbounded fluid is therefore commonly reduced to axisymmetric deformations invariant to the coordinate  $\phi$ , for which spherical harmonics are described by Legendre polynomials (called zonal harmonics). The axisymmetry property is commonly retained in theoretical works as simplifying mathematical derivations. In addition, some experiments based on axisymmetric external

<sup>\*</sup>maxime.fauconnier@inserm.fr

<sup>†</sup>jean-christophe.bera@inserm.fr

<sup>‡</sup>claud.inserra@inserm.fr

forcing [12], stereoscopic optical set-up [13] or coalescence-induced shape mode triggering [14] attest the validity of this assumption.

While microbubbles are commonly theoretically investigated as being immersed in an infinite liquid, constraints on bubble dynamics usually appear experimentally through the poking to neighboring cells [15], when being attached to a substrate in microfluidic applications [16–19], confined between walls [20] or restrained nearby a wall [3,21,22]. In the case of a wall-attached bubble, the interface temporal dynamics significantly differs from the free bubble theory. Even when considering the volume oscillations of a tethered bubble [23], the truncation of the bubble volume atop a substrate provides significant modification of the breathing mode pulsation as a function of the equilibrium contact angle. If the dynamic feature of the contact line motion is taken into account [24], then linear coupling between shape and volume oscillations has been evidenced for hemispherical bubbles. In this particular case, it is demonstrated that the only shape modes that may interact with the breathing oscillation are the axisymmetric ones (arbitrary  $n$ ,  $m = 0$ ). However, the triggering of nonaxisymmetric shape modes has already been demonstrated experimentally for ultrasound-driven bubbles [25] and vibrating drops [26,27]. For wall-attached microbubbles, the shape mode characterization is either performed through a Fourier mode decomposition of the bubble interface [17] (and hence restricted to axisymmetric deformations) or only qualitatively described [19,25]. In case of vibrating sessile drops, image postprocessing of profiles from a top view allows determining the modal decomposition on the basis of spherical harmonics [27]. In the above-mentioned studies the investigations are restricted to the shape mode classification, the temporal dynamics of the nonaxisymmetric oscillations being usually disregarded. The mechanism underlying which shape mode is chosen to grow to a steady state, and selected out, is not revealed so far. Such mode selection, and the establishment of a final bubble shape, may be deduced from the symmetry of the studied geometry [22] or preferential directions of the ultrasound wave [12]. Theoretically, a three-wave resonant interaction between the Faraday ripples on the bubble surface has been proposed to describe the selection of an established standing-wave pattern [28]. Experimentally, the preferential manifestation of sectoral modes has recently been described [19].

In this paper, an experimental approach is proposed with the view of studying the selection and temporal dynamics of nonspherical oscillations of a wall-attached bubble. In Sec. II, the experimental setup that allows capturing high-resolved temporal dynamics of an ultrasound-driven wall-attached bubble is described. In Secs. III, IV, and V, the identification and detection of asymmetrical shape oscillations are discussed. An image postprocessing method is then validated, enabling the modal analysis of an ultrasound-driven microbubble as a function of both its size and the increasing pressure of the acoustic field. Therefrom, the Sec. VI points out the modal nondegeneracy of spherical harmonics of a wall-attached bubble. Finally, Sec. VII draws particular attention to the interaction between zonal and sectoral modes and deepens the possible conditions for their coexistence.

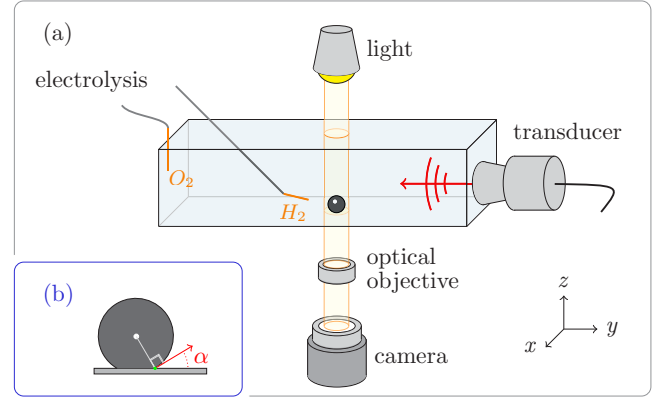


FIG. 1. (a) Schematic representation of the experimental setup. (b) Side view of the microbubble tethered at the tank's bottom, making a contact angle  $\alpha$  with the substrate in absence of ultrasound.

## II. METHODOLOGY

### A. Experimental setup

A schematic of the experimental setup is given in Fig. 1(a). Observations of ultrasound-driven microbubbles are performed in a polymethyl methacrylate tank of inner size  $L_x \times L_y \times L_z = 44 \times 260 \times 50$  mm. Experiments are conducted in pure (Milli-Q® IQ 7000) water supplemented with saline solution (NaCl concentration of  $24 \text{ mg/l} \pm 1 \text{ mg/l}$ ). A dihydrogen microbubble is created, resulting from a reduction reaction and occurring at the cathode of an electrolysis actuator. The electrolysis is actuated by a signal generator (Agilent 33210A, squared signal, peak-to-peak amplitude  $4V_{pp}$ , offset  $2V_{pp}$ , 50% duty cycle). When both cathode and anode, connected to the generator output, are dipped in water, bubbles made of dihydrogen are getting nucleated on the cathode tip. The cathode connector is tied to a three-axis hydraulic micromanipulator (Narishige MMO-203), which allows the positioning and tethering of the bubble at the tank's bottom. In this way, single bubbles of equilibrium radius ranging from  $60$  to  $230 \mu\text{m}$  may be nucleated for the purpose of this study.

The driving acoustic field is induced by a Langevin transducer (Reson, 30-kHz nominal frequency, high-voltage gain amplifier Trek50/750) located at one edge of the water tank. Acoustic coupling between the transducer and the water tank was ensured with ultrasound transmission gel (Aquasonic, Fisher ThermoScientific). Similarly to previous works investigating bubble shape deformations [29], bubbles are insonified by a sinusoidal signal modulated by a slowly varying envelope in order to generate the shape modes periodically: A triangle shape envelope of modulation frequency  $f_m = 25\text{Hz}$  is superimposed to a sine wave of frequency  $f_a = 30.5\text{kHz}$ . The visualization of the bubble's activity is performed using an inverted Nikon Eclipse-Ti microscope equipped with a  $10\times$  magnification optical lens. The bubble dynamics is captured by means of an high-speed camera (Vision Research, Phantom V12.1). The spatial resolution has been measured to be  $2 \mu\text{m}/\text{pixel}$ , thence a numerical inaccuracy of  $2 \mu\text{m}$ . Movies are performed with acquisition parameters (frame size, sampling frequency, and exposure time) that are bubble size dependent, as described in Table I. Such adjustment is

TABLE I. Acquisition parameters (frame size, sampling frequency, and exposure time) as set in the software Phantom Camera Control (PCC).

Bubble radius	Frame size	Sampl. frequency	Exp. time
$R_0 < 124 \mu\text{m}$	$128 \times 128$ pixels	180064 Hz	$4 \mu\text{s}$
$R_0 > 124 \mu\text{m}$	$256 \times 256$ pixels	67065 Hz	$7 \mu\text{s}$

necessary to optimize the field of view for a broad range of bubble radii.

### B. Acoustic field characterization.

The procedure to assess the acoustic pressure driving the bubble is the following. Considering that the modulation envelope is slowly varying, i.e.,  $f_m \ll f_a$ , the ultrasound field may be assumed to be a constant-amplitude sinusoidal signal during a few acoustic periods. At the beginning of the triangle modulation waveform, the acoustic pressure is low enough to induce relatively weak radial oscillations of the bubble. By capturing this radial dynamics and rearranging it on a single acoustic period, the obtained waveform can be numerically compared to a linearized Rayleigh-Plesset equation ruling the bubble spherical oscillations at low pressure. As all other parameters are known or can be measured directly (fluid viscosity and density, bubble equilibrium radius), the acoustic pressure can then be deduced from this modeling. This technique is reproduced for increasing driving voltage as far as the bubble interface remains spherical. Then acoustic pressures associated to bubble nonspherical oscillations are extrapolated linearly along the whole experimental data set. The applied pressures go to 40 kPa.

### C. Equilibrium bubble shape

Figure 1(b) shows a side view of a bubble attached to the substrate. The contact angle  $\alpha$  is defined by the angle between the tangent to the bubble surface at the contact point and the substrate plane. The value of this angle results from the wetting properties of water with the substrate and is ruled by the interface tensions that exist between the different media (gas, liquid, and solid). Therefore, the contact angle of the bubble at rest is independent of the bubble equilibrium radius. Measurements have been performed for a large number of single attached bubbles in a side-view configuration. The equilibrium contact angle was measured before ultrasound activation and equals  $54^\circ \pm 6^\circ$ .

## III. SHAPE MODES OBSERVATION

Applying an amplitude-modulated ultrasonic field results in a beating behavior of the spherical oscillations of the bubble, with a period  $f_m^{-1} = 40$  ms, and the variations of the radial mode  $a_{00}(t)$  alternate between low-amplitude and high-amplitude phases. During one modulation period, if the applied pressure exceeds the threshold of nonspherical oscillations, then the bubble interface deviates from sphericity. Typical examples of the recorded series of pictures are shown in Fig. 2 where the onset of nonspherical oscillations has

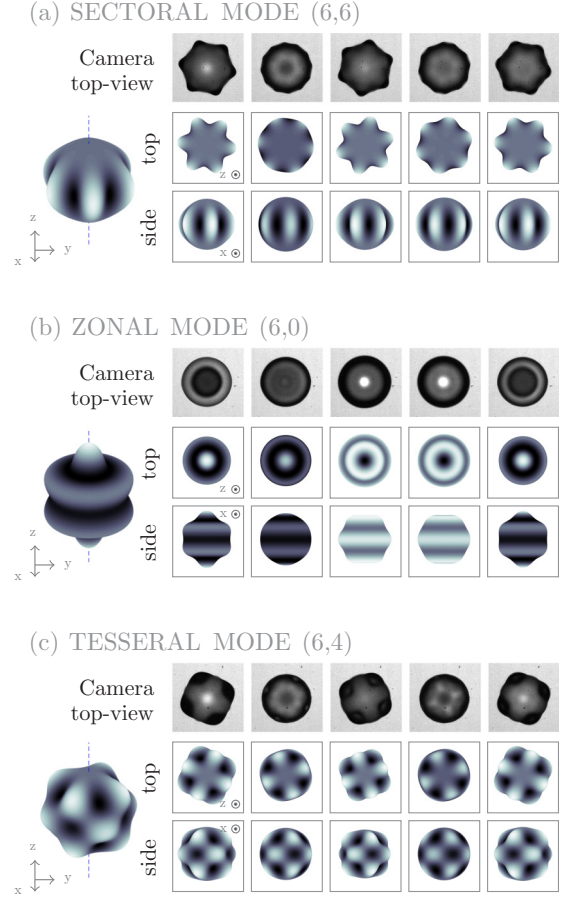


FIG. 2. Snapshot series of an experimental (camera top-view) bubble, with its associated theoretical spherical harmonics (top and side views), oscillating on a sectoral mode  $Y_{66}$  (a), on a zonal mode  $Y_{60}$  (b) and on a tesseral mode  $Y_{64}$  (c). The elapsed time between two consecutive snapshots is  $14.9 \mu\text{s}$ .

been reached. The bubble interface is captured from a top-view configuration. The snapshot series is plotted on two acoustic periods, revealing the subharmonic behavior of the nonspherical oscillation. We recall that, at first glance, no axisymmetry hypothesis can be made on the obtained bubble interface, and the bubble contour should consequently be decomposed over the set of spherical harmonics. The spherical harmonics are function of the spherical angle coordinates, the colatitude  $\theta \in [0 \pi]$  and the longitude  $\phi \in [0 2\pi]$ , and are written  $Y_{nm}(\theta, \phi) = f_{nm} P_{nm}(\cos\theta) e^{im\phi}$ , where  $P_{nm}$  is the associated Legendre polynomial of degree  $n$  and order  $m$ , and  $f_{nm} = \sqrt{\frac{(2n+1)}{4\pi} \frac{(n-|m|)!}{(n+|m|)!}}$  is a normalization coefficient. A set of bubbles exhibiting nonspherical oscillations on a spherical harmonic of degree  $n = 6$  is illustrated in Fig. 2. For each experimental snapshot series, the observed nonspherical mode is compared to top and side views of the corresponding theoretical spherical harmonic.

In Fig. 2(a) a bubble of equilibrium radius  $R_0 = 133.7 \mu\text{m}$  exhibits an easily recognizable contour with a six-lobe shape. This case illustrates the shape deformation along a sectoral harmonic  $Y_{66}$  for which the top view corresponds to a  $n$ -lobe deformation. From the side view, a sectoral harmonic is close

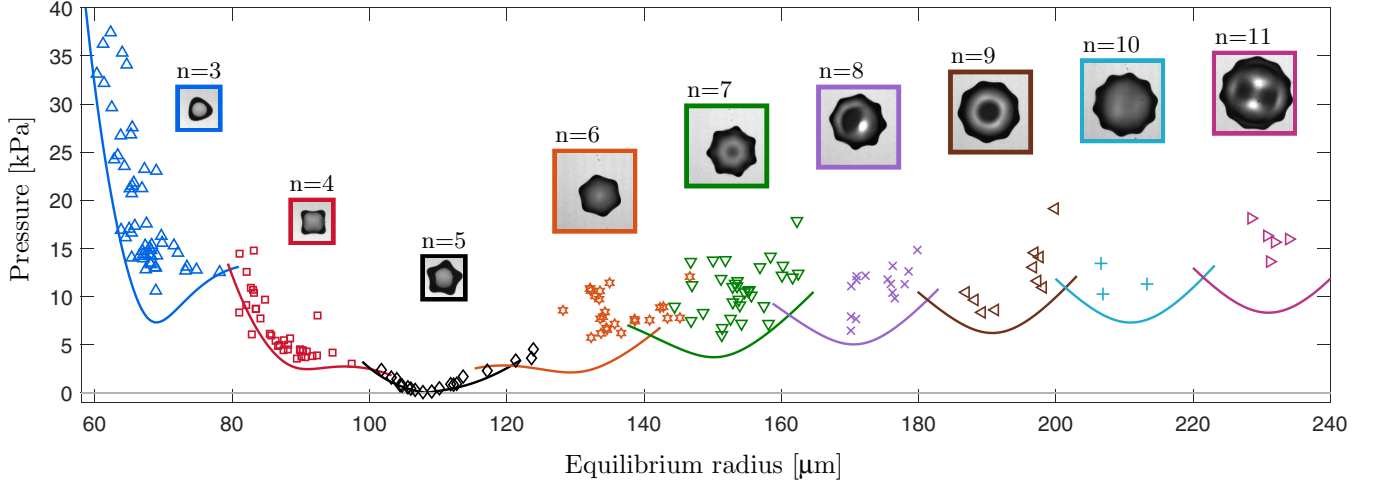


FIG. 3. Instability thresholds of sectoral harmonics ( $m = n$ ) as a function of the bubble equilibrium radius. Experimental wall-attached bubbles (geometric markers) are compared with free bubble theory (continuous lines), according to Refs. [10,11]. Depending on the bubble size, the frame dimension varies following Table I.

to a spherical shape as the associated Legendre polynomial can be reduced to  $P_{nm}(\cos\theta) \sim \sin^n(\theta)$ , that is a bell-shape function with zero values at the poles. In Fig. 2(b) a bubble of equilibrium radius  $R_0 = 131.5 \mu\text{m}$  exhibits spherical oscillations from the top view, with some additional interface motion along the elevation visible due to optical effects. This case illustrates the shape deformation along a zonal harmonic  $Y_{60}$ . Zonal harmonics are axisymmetric functions: Their contour looks spherical from a top view and their shape deformation from the side view is a Legendre polynomial ( $m = 0$ ). At first, identifying this axisymmetric shape uniquely from the top view is not straightforward. Finally Fig. 2(c) illustrates the shape deformation along a tesseral spherical harmonic  $Y_{64}$  for a bubble with equilibrium radius  $R_0 = 131.3 \mu\text{m}$ . In this case the shape deformation becomes more complex with angular deviations from the sphere along the elevation and azimuthal directions. It is worth noting that a  $Y_{nm}$  spherical harmonic possesses  $n - m$  nodal lines along the elevation. Between each nodal lines the azimuthal shape is governed by a  $\cos(m\phi)$  function, and due to the phase interplay from two successive nodal lines the azimuthal shape is out of phase with the previous one. The top-view integration of a  $Y_{nm}$  tesseral harmonic provides a seemingly  $2m$ -lobe bubble contour. In the case illustrated in Fig. 2(c), the nonspherical mode  $Y_{64}$  shows indeed an eight-lobe top-viewed contour. Among the possible nonspherical oscillations decomposed over the zonal, tesseral, or sectoral harmonics, bubbles oscillating along a sectoral harmonic ( $m = n$ ) are the ones easily recognizable in a top-view configuration. By decomposing the bubble contour on a  $\cos(n\phi)$  function, the onset of a sectoral harmonic may be deduced during the amplitude-modulated pressure driving, leading to the instability threshold for this particular asymmetric oscillation.

#### IV. DEGREE $n$ DIFFERENTIATION

The detection of the emergence of sectoral harmonics has been performed for approximately two hundred bubbles of radius in the range  $[60 \text{ } 230] \mu\text{m}$ . Note that because our

experiments are conducted at a fixed driving frequency, the excited shape mode mainly depends on the bubble size and driving pressure amplitude. All results are presented in a radius-pressure map in Fig. 3. Bubbles showed nonspherical oscillations on sectoral harmonics with degree ranging from  $n = 3$  to  $n = 11$ . The analysis of their temporal evolution revealed that they oscillate at half the driving frequency and, consequently, are all triggered on their first parametric resonance. Figure 3 highlights the fact that each degree- $n$  sectoral oscillation is exclusively associated to a specific range of bubble size. This nonoverlapping feature is similar to the partitioning of axisymmetric modes related to their bubble radii [14]. We therefore compare the experimental instability threshold for sectoral harmonics to the theoretical ones obtained in case of axisymmetric shape oscillations of free bubbles. The degree- $n$  free bubble instability threshold  $P_{\text{th}}^n$  can be obtained from asymptotic approximation of the set of equations ruling the oscillations of axisymmetric deformations [10,11], and is expressed as:

$$P_{\text{th}}^n = \rho R_0^2 C_n \sqrt{(\omega_B^2 - \omega_0^2)^2 + \omega_0^2 \delta^2}, \quad (3)$$

where

$$C_n = \frac{(a-1)^2 + 4p}{\sqrt{\left[-\frac{3}{2}a + 2p + 2\left(n + \frac{1}{2}\right)\right]^2 + q^2}},$$

and

$$a = \frac{4(n-1)(n+1)(n+2)\sigma}{\rho\omega_0^2 R_0^3},$$

$$p = \left[ \frac{2(n+2)(2n+1)\mu}{\rho\omega_0 R_0^2} \right]^2,$$

$$q = \frac{6(n+2)\mu}{\rho\omega_0 R_0^2},$$

and  $\mu$  is the viscosity of the medium,  $\omega_0$  is the driving pulsation,  $\omega_B$  is the resonance frequency of the bubble volumetric



mode,  $\delta = \frac{4\mu}{\rho R_0^2}$  is the damping constant applied by the medium on the bubble, and  $n$  is the modal degree.

As shown in Fig. 3, the theoretical instability thresholds for zonal harmonics  $Y_{n0}$  of free bubbles allow recovering the splitting of the onset of sectoral harmonics  $Y_{nm}$  of tethered bubbles, with the bubble radius, for the same  $n$  values. In addition, all experimental results are located close to or above the respective  $Y_{n0}$  theoretical curve of free bubble. This behavior respects the theoretical assumption that proposes that, for a set of degree- $n$  spherical harmonics, every order- $m$  nonspherical modes are triggered above the same instability threshold [10].

## V. ORDER $m$ DIFFERENTIATION

### A. Identification process

Due to the partitioning of the degree- $n$  spherical harmonics with the bubble equilibrium radius, we may postulate that the index  $n$  is known once the bubble radius is measured. Therefore specific strategies can be designed to extract the value  $m$  of a given spherical harmonic, paving the way to the differentiation of the set of zonal, sectoral, and tesseral harmonics. We recall that, from a top view, the appearance of zonal harmonics  $Y_{n0}$  results in a circular contour. The differentiation of this nonspherical oscillation from a purely radial one is performed through the analysis of its subharmonic behavior. It is worth noting that this feature differs from the very similar case of a vertically vibrated sessile drop, for which the zonal mode must synchronize with the driving base and oscillate at the fundamental [27]. In the same way, the appearance of a sectoral harmonic  $Y_{nm}$  results in a  $n$ -lobe contour in top view. This shape oscillates at half the driving frequency due to parametric excitation. The combination of the spatial (contour) and temporal (subharmonic) information on a  $\cos(n\phi)$  projection confirms the existence of a sectoral mode. The main difficulty lies in the identification of a tesseral ( $0 < m < n$ ) mode. As discussed in Sec. III and Fig. 2, a spherical harmonic possesses  $n - m$  azimuthal nodal lines due to the property of the associated Legendre polynomial  $P_{nm}$ . When  $n - m \neq 0$ , the phase interplay between successive nodal lines induces the top-view contour to have a seemingly  $2m$ -lobe shape. More exactly it consists of two sets of  $m$ -lobe disposed in a staggered arrangement, whose amplitude may differ according to the parity of  $n - m$ . This property is illustrated in Fig. 4 and discussed here with two exemplary cases.

When  $n - m$  is even, the bubble interface is symmetric with respect to the equatorial plane  $\theta = \pi/2$ . The top-view contour exhibits a  $2m$ -lobe shape, consisting of two sets of  $m$ -lobe shape with different amplitudes. This behavior results in two spatial harmonic components (referred as  $\phi$  components in what follows) of the azimuthal contour  $r(\phi, t)$  at the frequencies  $m$  and  $2m$ . This is highlighted in Fig. 4(a) for a  $Y_{64}$  tesseral harmonic. In addition it can be shown that the  $\phi$ -component  $m$  oscillates temporally at the subharmonic frequency  $f_0/2$ , while its spatial harmonic  $2m$  oscillates at the driving frequency. This temporal characteristic allows especially the differentiation of an order- $m$  tesseral harmonic from a sectoral harmonic in the special case  $n = 2m$ , for which the spatial  $\phi$ -component  $n$  oscillates at  $f_0/2$ .

When  $n - m$  is odd, the bubble interface exhibits a nodal line along the equatorial plane. The top-view contour exhibits

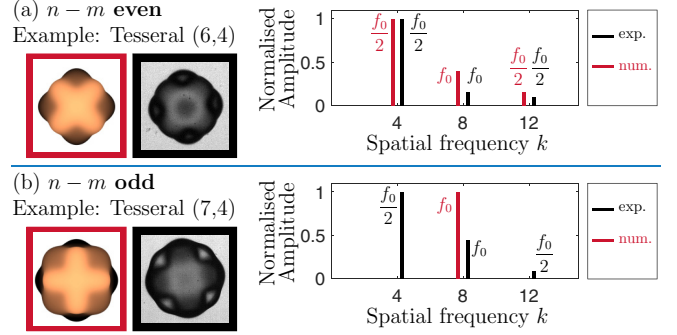


FIG. 4. Change in spectral signature due to nodal lines parity. Spatiotemporal Fourier decomposition of the bubble contour  $r(\phi, t)$  (normalized amplitude), processed for numerical (in red) and experimental (in black) cases of spherical harmonics  $Y_{64}$  (a) and  $Y_{74}$  (b). The discrepancy between numerical and experimental cases comes from the ombroscopic-induced artefact that affects the optical image but not the numerical projection. This is amplified in the  $n - m$  odd situation due to the existence of a nodal line along the equatorial plane.

then a  $2m$ -lobe shape, consisting of two sets of  $m$ -lobe with equal amplitudes. The spatial projection of the azimuthal contour  $r(\phi, t)$  mainly contains the  $\phi$ -component  $2m$ , oscillating at the driving frequency. This is shown in Fig. 4(b) for a  $Y_{74}$  tesseral harmonic. In this case the numerical projection of the bubble interface is reduced to the  $\phi$ -component  $2m = 8$ . The identification of the order  $m = 4$  is thus not straightforward. Fortunately, experimental conditions always contain the  $\phi$ -component  $m$  due to the ombroscopic image sharpness, which naturally induces some difference in lobe amplitudes depending on their position in elevation, as shown in Fig. 4.

In conclusion, the combined spectral analysis along both space and time allows the differentiation of the order  $m$  of any spherical harmonics and is particularly convenient for the detection of tesseral harmonics, for which the geometric identification is not straightforward. This process is implemented through a spatial Fourier transform of the top-view bubble contour  $r(\phi, t)$  along the angular coordinate  $\phi$ :

$$c_{nk}(t) = \int_0^{2\pi} r(\phi, t) e^{-ik\phi} d\phi, \text{ with } 0 \leq k \leq 2n, \quad (4)$$

where  $c_{nk}(t)$  is the modal coefficient associated to the  $\phi$ -component  $k$  of degree  $n$ . According to the above-mentioned identification process of the order- $m$  tesseral harmonics, each  $c_{nk}(t)$  coefficient is further filtered around the driving frequency  $f_0 = 30.5$  kHz and the subharmonic  $f_0/2 = 15.25$  kHz. For each mode  $Y_{nm}$ , the spatial harmonic  $k = 2m$  is used for the identification of its order  $m$ , while the  $k = m$  coefficient  $c_{nm}(t)$ , oscillating at  $f_0/2$ , is presented in the following as its modal amplitude. It is worth noting that this modal coefficient differs from the theoretical one  $a_{nm}$ , as defined in Eq. (1), due to a bias in the projection's decomposition.

### B. Numerical validation

A validating example of the proposed identification process is performed through the numerical analysis of the bubble nonspherical dynamics and its top-view contour. A virtual

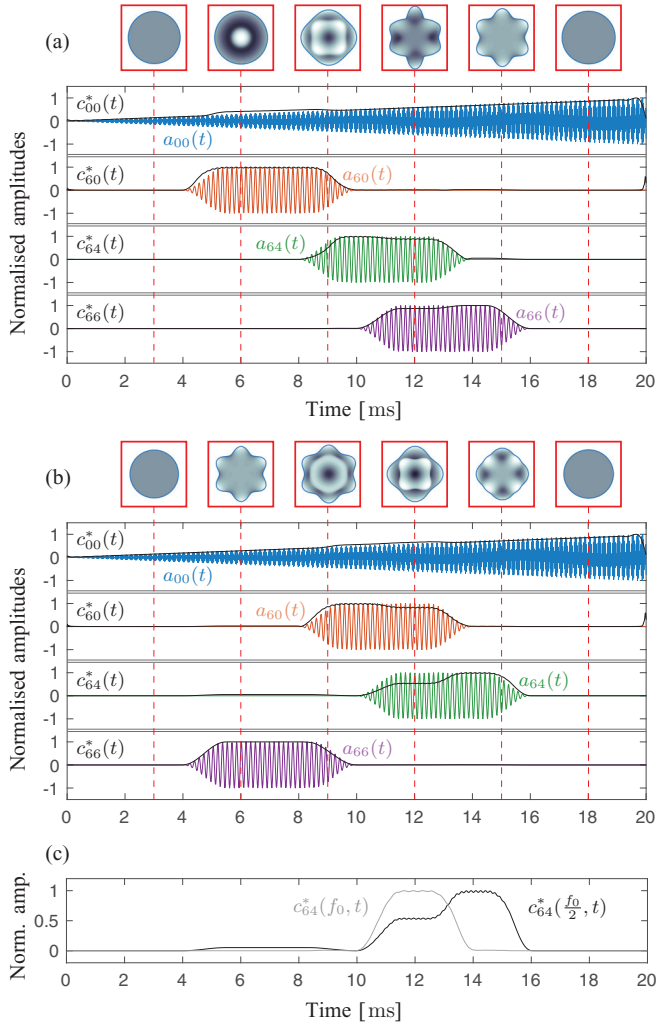


FIG. 5. Modal decomposition of a top-view bubble contour including the  $Y_{60}$ ,  $Y_{64}$ , and  $Y_{66}$  modes triggered at time  $(t_0, t_4, t_6)$  superimposed to a breathing mode  $Y_{00}$ . Comparison of the coefficients  $c_{nm}^*(t)$  with the theoretical ones  $a_{nm}(t)$  in case of (a)  $(t_0, t_4, t_6) = (4, 8, 10)$  ms and (b)  $(t_0, t_4, t_6) = (8, 10, 4)$  ms. (c) Evidence of amplitude transfer between the subharmonic  $c_{64}^*(\frac{f_0}{2}, t)$  and fundamental  $c_{64}^*(f_0, t)$  coefficients of the  $Y_{64}$  tesseral mode.

bubble of arbitrary equilibrium radius  $R_0$  is submitted to a sine wave modulated by a ramp envelope. The bubble interface is implemented as follows:

$$r(\theta, \phi, t) = R_0 + \frac{t}{\tau} a_{00}(t) Y_{00} + \sum_{n \neq 0, m} a_{nm}(t) Y_{nm} H_T(t - t_m), \quad (5)$$

where  $a_{nm}(t) = a_{nm} \cos(\pi f_0 t)$  and  $a_{00}(t) = a_{00} \cos(2\pi f_0 t)$  are the time-varying amplitudes of, respectively, the subharmonic nonspherical modes and the radial mode,  $\tau = 20$  ms is the signal duration and  $H_T$  is the Hanning operator of duration  $T = 6$  ms centered at time  $t_m + T/2$ . Figures 5(a) and 5(b) presents two modal decomposition of a bubble interface exhibiting a breathing mode  $a_{00}$ , as well as zonal  $Y_{60}$ , sectoral  $Y_{66}$  and tesseral  $Y_{64}$  harmonics. The case in Fig. 5(a) [respectively, Fig. 5(b)] corresponds to the onset times  $(t_0, t_4, t_6) = (4, 8, 10)$  ms [respectively,  $(8, 10, 4)$  ms]. Numerical top-view

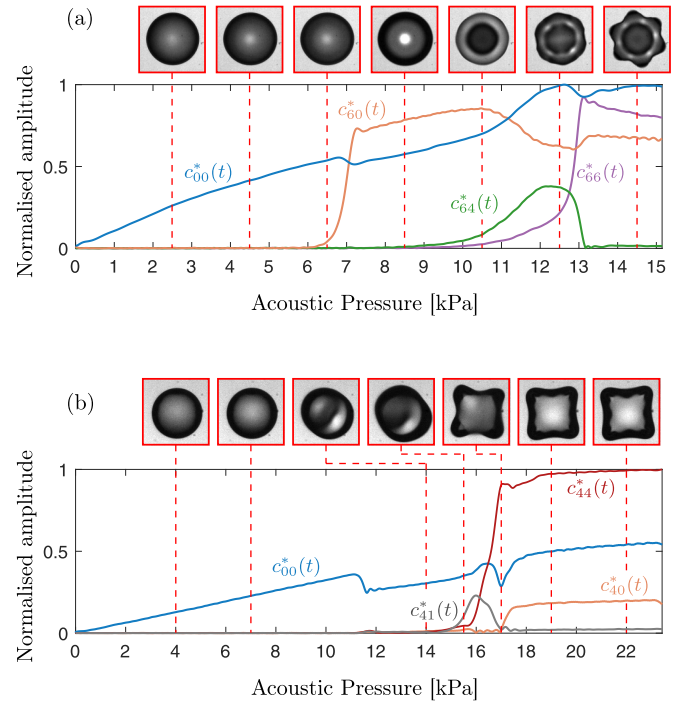


FIG. 6. Evolution of the modal coefficients  $c_{nm}^*(t)$  resulting from a top-view contour in the case of a bubble (a) with equilibrium radius  $R_0 = 133 \mu\text{m}$  oscillating on the set of  $n = 6$  spherical harmonics and (b) with equilibrium radius  $R_0 = 83 \mu\text{m}$  oscillating on the set of  $n = 4$  spherical harmonics. Only the predominant nonspherical modes are displayed. Snapshot series illustrate significant changes in bubble shape.

snapshots of the bubble contour allow illustrating the shape deformation induced by these nonspherical oscillations. The result of the spatiotemporal analysis of the bubble contour is provided by the envelopes  $c_{nm}(t)^*$  of the modal coefficients  $c_{nm}(t)$  oscillating at the subharmonic of the driving frequency. For both cases the onset times of the implemented nonspherical modes appear correctly tracked and defined. The maximal amplitudes of the oscillations is in good agreement with the theoretical ones, except in two circumstances. The first one concerns the quantification of the radial oscillation when a zonal harmonic appears, leading to a slight overestimation of the breathing mode amplitude. The second one concerns the amplitude of the tesseral harmonic  $Y_{64}$  when combined to another nonspherical mode [Figs. 5(a) and 5(b)]. In this case a part of the modal amplitude is contained into the  $2m$  frequency component oscillating at the driving frequency, in accordance to the proposed spatiotemporal analysis and filtering. This amplitude transfer between  $c_{64}(f_0, t)^*$  and  $c_{64}(\frac{f_0}{2}, t)^*$  for the second exemplary case is illustrated in Fig. 5(c).

### C. Bubble vibration sequence

The spatiotemporal analysis is applied to an experimental case. This allows characterizing the bubble vibration sequence consisting of the set of successively triggered nonspherical modes. Figure 6 presents two experimental wall-attached bubbles of equilibrium radii 133 and  $83 \mu\text{m}$  that deviate from

spherical shape in the set of  $n = 6$  and  $n = 4$  spherical harmonics, respectively. In addition to snapshot series of the top-view contour, the envelopes  $c_{nm}^*(t)$  of the modal coefficients that are dominantly excited are shown. The bubble interface presented in Fig. 6(a) follows the successive vibration sequence  $Y_{60} - Y_{64} - Y_{66}$  once nonspherical oscillations appear. The existence of these modes is clearly visible on the top-view snapshots, giving confidence into the proposed analysis. When the zonal mode emerges, the amplitude of the radial oscillation decreases. This phenomenon can be associated to a possible energy transfer between modes [29] but also to a bias in the determination of the amplitude of the modal coefficient  $c_{nm}(t)$ . Therefore the analysis of mode coupling is not straightforward at this stage. It is worth noting that the existence of the  $Y_{64}$  tesseral harmonic is short and precedes the onset of the sectoral oscillation.

The bubble interface presented in Fig. 6(b) follows the successive vibration sequence  $Y_{41} - Y_{44} - Y_{40}$  once nonspherical oscillations appear. The fact that the  $Y_{41}$  tesseral harmonic is the first mode to be triggered is clearly visible on the snapshot series. Once more, the existence of the tesseral harmonic is short and precedes the onset of both sectoral and zonal modes. By the way, Fig. 6(b) shows that both sectoral and zonal modes follow similar trends and reach a plateau value of oscillation amplitude.

## VI. MODAL NONDEGENERACY

### A. Instability thresholds

The analysis of the bubble vibration sequence has been performed over the whole data set of experimental wall-attached bubbles, leading to the determination of the onset of the first triggered nonspherical oscillation. These pressure thresholds are displayed in a pressure-radius map, for subresonant radii (degree  $n = 3$  and  $n = 4$ ) in Figs. 7(a) and 7(b) and for overresonant radii (degree  $n = 7$ ) in Fig. 7(c), respectively. In Fig. 7 each geometrical marker is associated to a particular vibration sequence and indicates the pressure value at which the bubble interface diverges from the purely radial mode. In addition, the color range points out which nonspherical mode is first triggered.

In order to help in the figure readability, parabolic-like graphical fits have been drawn for each order- $m$  mode, for  $m = 0$  to  $n$ , and allow identifying their respective zones of bubble shape instability or resonance bands. For low degrees ( $n = 3$  or  $4$ ), these resonance bands only slightly overlap. For higher degree ( $n = 7$ ), despite a strong overlap, some orders  $m$  appear completely distinct. More precisely, for each investigated degree  $n$ , three distinct modal regions are found. In the vicinity of the nonspherical resonant radius of the equivalent free bubble [given by the radius at which a degree  $n$  is parametrically excited, see Eq. (1)], zonal and sectoral modes emerge preferentially. Far from this resonant radius, tesseral modes are most likely to show up first. We therefore distinguish the degree- $n$  modal regions as a three-band zone, the tesseral-mode bands surrounding the zonal and sectoral ones. We can be confident in this result, since the frequency of the sectoral mode, compared to other nonspherical mode of a same modal subset of spherical harmonics, is the less likely

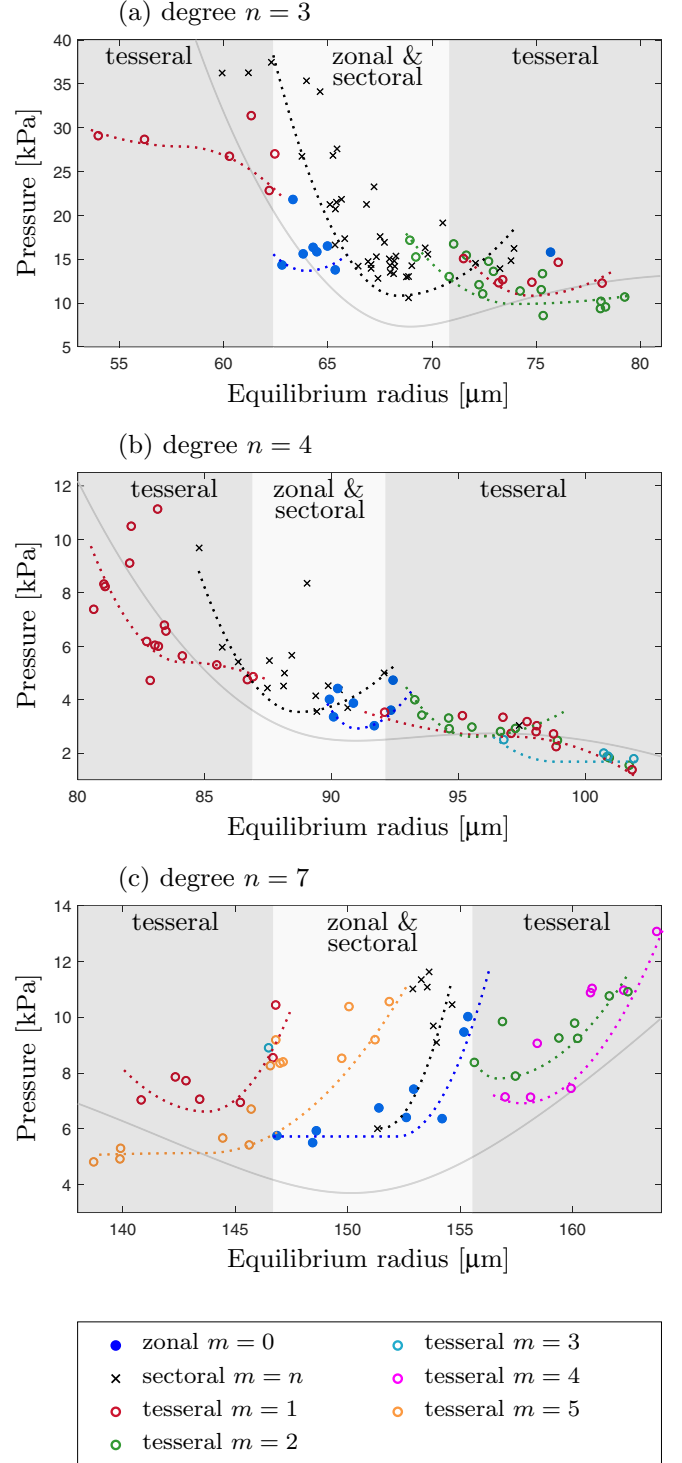


FIG. 7. Instability pressure thresholds of the first triggered nonspherical shape modes of degree  $n = 3$  (a),  $n = 4$  (b), and  $n = 7$  (c). Parabolic-like graphical fits (dashed lines) give an overview of the nondegenerate instability threshold curves. The continuous gray lines are the theoretical instability curves of free axisymmetric bubbles [10,11], centered on the respective modal resonances.

to differ as a function of the equilibrium contact angle [30]. Contrariwise to the Lamb spectrum where every modes  $m$  of a same degree  $n$  have the same resonance frequency, the experimental instability curves of Fig. 7 unveil resonant radius that

are order dependent. This evidences a modal nondegeneracy over the set of zonal, tesseral, and sectoral modes. Such modal nondegeneracy has already been observed experimentally for vibrating sessile drops [27] and demonstrated theoretically for levitating drops with the appearance of  $n + 1$  modal regions for a given degree  $n$  of the parametrically excited nonspherical mode [31]. To our knowledge the modal nondegeneracy of bubble asymmetrical oscillations has not been demonstrated so far.

### B. Occurrence of specific orders $m$

It is worth mentioning that asymmetric bubble shapes only arise from a break into the problem symmetry, usually caused by a geometrical singularity [22] or by asymmetry in the external forcing [12]. Moreover, which nonspherical mode is selected under external forcing for a given bubble radius has not been explained theoretically. In the present investigation, because of the pinning of the bubble on a substrate, specific nonspherical oscillations may encounter difficulties to be triggered, while other modes would experience the pinning as less inhibiting. At first glance, it is reasonable to suppose that a zonal mode, with a circular contact line shape and a possible nodal line matching the contact, is more inclined to emerge at low acoustic pressure. Concerning sectoral modes, the conditions of their emergence are less obvious as the contact line or angle are necessarily changing, if conform with the free bubble modal shapes. Nevertheless, the sectoral shape of a superhemispherical wall-attached bubble would always encounter *weak* variations of contact line and angle with respect to the equilibrium state. On the contrary, tesseral modes should encounter much greater variations of contact line and angle, while, for a given contact angle, some of them can have a nodal line matching the contact, which would strongly condition their respective emergence. This might explain why certain tesseral modes have never been observed in the present experimental setup, while others never miss to show up.

Substantial literature exists for the modal analysis of sessile drops [24,26,27,30,32]. It has been demonstrated that, for sessile drops, the modal content of the nonspherical drop shape relies on the equilibrium contact angle and the contact line mobility [30]. At very high mobility, the contact line motion is facilitated while the instantaneous contact angle barely varies. The substrate-induced stress is less constraining. The dynamics of the system approaches the one of a free drop, displaying degenerate Lamb natural frequencies, as defined by Eq. (2). At low mobility, the contact line moves hardly and its dynamics is ensured by more extreme contact angles. Therefore this mobility limitation leads to stronger interface deformations, facilitating the onset of nonspherical shapes [33]. As a consequence, a modal splitting is expected and has been experimentally observed [30]. Modal nondegeneracy is shown to occur when the equilibrium contact angle  $\alpha$  differs significantly from  $90^\circ$ , in other words when the undisturbed drop shape is no longer hemispherical [32]. The degeneracy break yields to frequency reordering and modal crossing, responsible for coexistence between modes [30], and eventually for coupling between resonant modes. When regarding the investigated bubble with measured contact angle about  $54^\circ \pm 6^\circ$ , the undisturbed shape is far from being

hemispherical. Similarly to the case of sessile drops, it favors the mode coupling (Sec. V), modal nondegeneracy (Sec. VI and Fig. 7) and coexistence (Sec. VII and Fig. 8).

In addition, it is shown that the resonance frequency of sectoral modes does not differ significantly from the one of zonal modes. Accordingly sectoral modes have been often reported because of their ease to emerge at low pressure amplitude. Recently, the contact line dynamics and mobility, and their impact on the onset of nonspherical modes have been modelled numerically for the case of a tethered bubble submitted to increasing acoustic pressure [19]. Preferential triggering of the sectoral mode over the other nonspherical oscillations have been shown, but only in a qualitative way. From a theoretical point of view, Maksimov [28] derived the conditions of the emergence of specific shape mode patterns in order to clarify experimental observations of nonspherical bubble interface [34]. The theoretical model relies on the Faraday wave analysis over the bubble interface, based on a triad resonant interaction between the radial mode and two shape modes. The preferential triggering of peculiar patterns called rolls (sectoral shape) and squares (combination of sectoral and zonal modes) is highlighted but is limited to the case of high modal degree ( $n > 9$ ).

## VII. COEXISTENCE OF ZONAL AND SECTORAL MODES

It is worth noting that the theoretical derivations of Maksimov [28] concern the emergence of specific patterns that are either the combination of zonal and sectoral harmonics, either a lone sectoral harmonic. In the present study, for bubble radii near the nonspherical resonant radius of a given degree  $n$ , we take advantage of the previously described spatiotemporal image processing method for mode differentiation in the aim of analyzing the dynamics of zonal and sectoral modes. The modal amplitudes and nonspherical deformations of the radial, zonal and sectoral modes are exposed for odd degree modes in Figs. 8(a) and 8(b) and for even degree modes in Figs. 8(c) and 8(d). The normalized modal coefficients  $c_{nm}^*(t)$  and  $c_{nm}(t)$  are depicted respectively during a complete modulation period and during two acoustic periods. In addition, schematics of the bubble interface for each considered shape mode is provided.

Literature about a vibrating sessile drop reports two kinds of modal interaction: “mode mixing” and “mode competition” [32]. It is demonstrated that two modes are more inclined to hysteretically compete when their resonance bands intersect or when they are oscillating at the same harmonic frequency. Otherwise, they both display an unconstrained linear superposition of their respective dynamics. Contrarily to the present experiment, it should be pointed out that sessile drops are usually excited by a substrate-normal driving. This leads to the triggering of zonal modes oscillating at the fundamental frequency and to nonzonal modes exhibiting a subharmonic response. On the contrary the nonspherical modes developing on the interface of wall-attached bubbles are all parametrically excited, hence oscillating at half the driving frequency. In addition to the recurrent overlapping of the resonance frequency bands of zonal and sectoral modes (cf. Fig. 7), this suggests that “mode competition” would be more likely to occur if we refer to Ref. [32]. However, Fig. 8 unveils



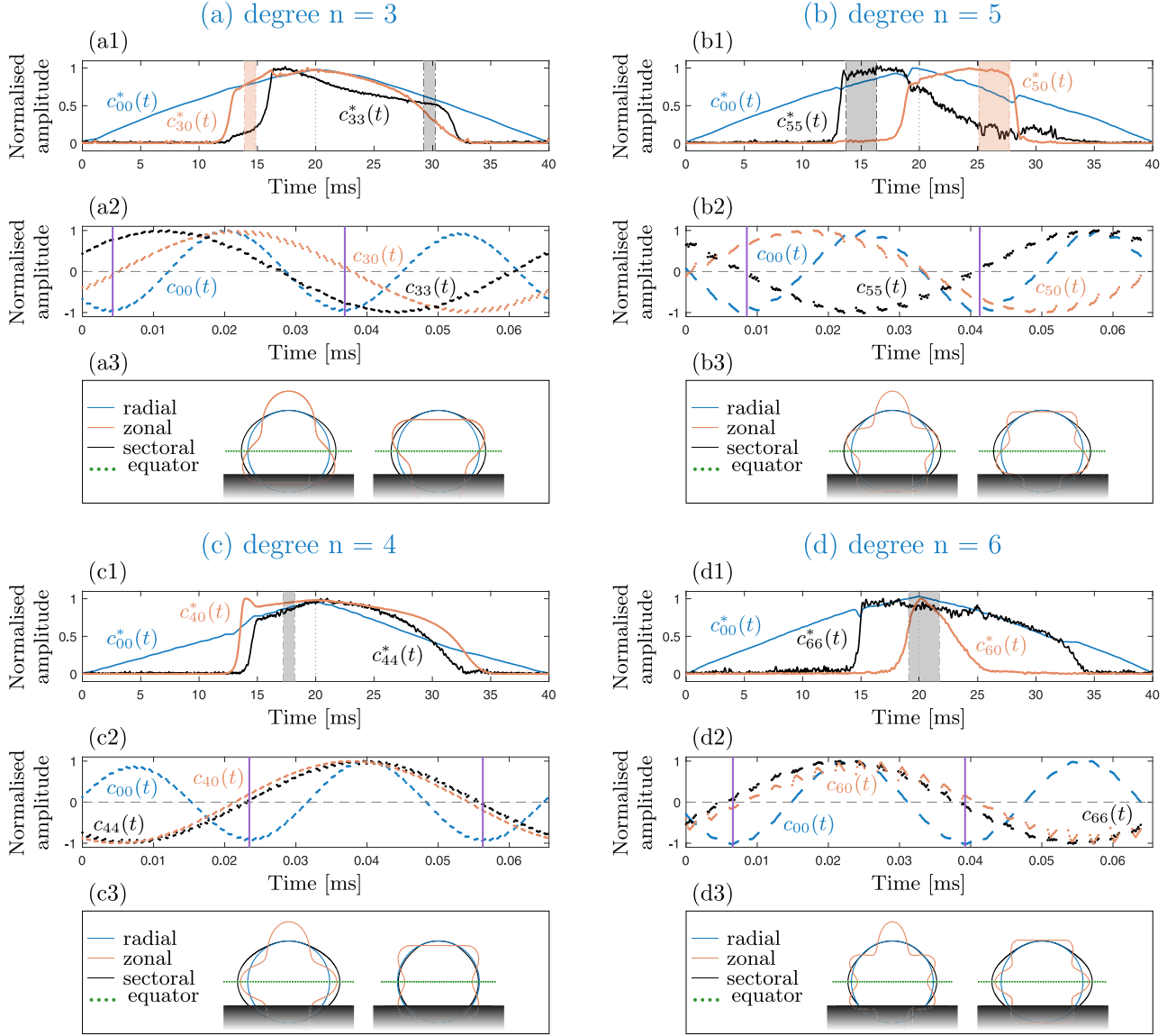


FIG. 8. Coexistence of sectoral and zonal modes is exposed relying on their modal interplay, phase relation and symmetry compatibility for the cases of modes of odd degree  $n = 3$  (a) and  $n = 5$  (b) and even degree  $n = 4$  (c) and  $n = 6$  (d). For each case (x), the information is structured as follows. (x1) Evolution of the coefficients  $c_{nm}^*(t)$  for the radial, zonal and sectoral modes along a complete modulation period; (x2) evolution of the oscillatory behavior of the coefficients  $c_{nm}(t)$  for the same modes, taken at particular times corresponding to coloured areas in (x1) and refolded over two acoustic periods. vertical purple lines correspond to the instants where occur the minima of radial oscillation; and (x3) side-view schematics of the extrema of bubble deformations for the selected shape modes.

dissimilarities in the modal interaction depending on the degree  $n$ , as described in the next two paragraphs through an original approach highlighting their modal dynamics, amplitude interplay and phase relation, and their geometric compatibility.

In Figs. 8(c) and 8(d) where even degrees  $n = 4$  and  $n = 6$  are detailed, sectoral and zonal modes exhibit stable coexistence: Their modal oscillation amplitudes reach a plateau value without inhibiting each other. This corresponds to “mode mixing,” as their modal envelopes  $c_{nk}^*(t)$  display an unconstrained linear superposition. This aspect is illustrated in Figs. 8(c1) and 8(d1). In addition, the observation of their dynamics reinforces this interpretation. Indeed,

very interestingly, Figs. 8(c2) and 8(d2) reveals the obvious synchronization of the zero crossing of their respective nonspherical deformations with the minimum of the radial oscillation (graphically marked with vertical purple lines). This probably happens as a way to minimize the magnitude of bending energy. As a consequence, it is also worth noting that zonal and sectoral modes oscillate then in-phase. As a matter of fact, both zonal and sectoral modes seem to synchronize independently with the radial mode, given that this occurs similarly when one of them is lonely triggered. Last, Figs. 8(c3) and 8(d3) depict side-view schematics of the corresponding bubble deformations. From a geometrical point of view, both zonal and sectoral deformations of even

degree possess a vibration anti-node at the equatorial plane of the bubble, which could explain their propensity to coexist.

In contrast, in Figs. 8(a1) and 8(b1), it appears that zonal and sectoral modes of odd degree  $n = 3$  and  $n = 5$  do not emerge simultaneously. The onset of the secondly triggered mode seems to coincide with the fading of the first one, as it is clearly visible in the case  $n = 5$ . This corresponds to “mode competition,” as their modal interaction is characterized by the domination of some mode and by a challenging coexistence. The first triggered nonspherical shape modes, zonal (3,0) coded in orange in Fig. 8(a) and sectoral (5,5) coded in black in Fig. 8(b), are spontaneously privileged and show similar behavior, namely the synchronization of the zero crossing of their nonspherical deformations with the minimum of the radial oscillation (graphically marked with vertical purple lines). The secondly triggered nonspherical shape modes, sectoral (3,3) coded in black in Fig. 8(a) and zonal (5,0) coded in orange in Fig. 8(b), arrive later. They never encounter a possibility to oscillate in-phase with the first triggered modes and favor a synchronization of their zero crossing of nonspherical deformations with a zero crossing of the radial oscillation. Still from a geometrical point of view, as schematized in Figs. 8(a3) and 8(b3) for this odd degree case, the equatorial plane corresponds to a vibration antinode of the sectoral mode but to a vibration node of the zonal shape. Hence both sectoral and zonal modes undergo conflicting shapes. This could explain why modal competition occurs and why they never exhibit an in-phase behavior.

However, this does not explain their specific and recurrent phase-locking relation, determine how coupling operates, or even justify the legitimacy for one mode to dominate another. Explaining the modal coexistence would most likely involve a multiparameter study and not just an investigation of the shape compatibility, the contact line, or the phase relation. In definitive, it would be worth investigating whether the phase relation is rather governed by a minimization of the energy cost occurring at the contact. Such an analysis would require access to the contact line dynamics and mobility, as well as to both the macroscopic and the microscopic behaviors near the contact of a wall-attached bubble excited on nonspherical

shape modes. So far, these remain experimentally very difficult to obtain. Nevertheless, we are confident in saying that the phase relation between zonal and sectoral modes is essential for their coexistence as a means of minimizing in some way their energy cost.

## VIII. CONCLUSION

In the absence of any consistent theoretical model for the dynamics of an ultrasound-excited wall-attached bubble and the triggering of its surface instability, we proposed an experimental study with the aim of investigating the modal behavior of such a bubble under acoustic excitation. The vibration sequence of a bubble oscillating on nonspherical shape deformations is obtained from a spatiotemporal analysis of its top-view contour. The differentiation of any nonspherical shape modes led to the mapping of their pressure instability threshold as a function of the bubble size. This revealed for the first time, as far as we know, the nondegeneracy of the set of nonspherical shape modes of a wall-attached bubble as a three-band zone of modal resonances, with a preferential triggering of sectoral and zonal modes around the free bubble resonant radius and a triggering of tesseral modes further than this resonant radius. Finally, an original investigation of the coexistence between zonal and sectoral modes explores their modal interaction in terms of their amplitude interplay, phase relation, degree parity, and symmetry compatibility. Similarly to sessile drops but, in the present study, observed for the case of a wall-attached bubble, two kinds of modal interaction behavior are reported: Sectoral and zonal modes of even degree  $n = 4$  and  $n = 6$  show ease of coexistence and preferential “mode mixing,” while sectoral and zonal modes of odd degree  $n = 3$  and  $n = 5$  present greater difficulties to exist simultaneously, given that important “mode competition” occurs.

## ACKNOWLEDGMENTS

This work was supported by the LabEx CeLyA of the University of Lyon (ANR-10-LABX-0060/ANR-11-IDEX-0007).

- 
- [1] Z. C. Feng and L. G. Leal, *Annu. Rev. Fluid. Mech.* **29**, 201 (1997).
  - [2] P. L. Marston, *J. Acoust. Soc. Am.* **67**, 1 (1980).
  - [3] X. Xi, F. Cegla, R. Mettin, F. Holsteyns, and A. Lippert, *J. Acoust. Soc. Am.* **135**, 1731 (2014).
  - [4] G. Lajoinie, I. de Cock, C. C. Coussios, I. Lentacker, S. le Gac, E. Stride, and M. Versluis, *Biomicrofluidics* **10**, 011501 (2016).
  - [5] Z. Fan, R. E. Kumon, and C. X. Deng, *Ther. Deliv.* **5**, 467 (2014).
  - [6] Y. Kung, C. Lan, M. Hsiao, M. Sun, Y. Hsu, A. P.-H. Huang, W. Liao, H. Liu, C. Inserra, and W. Chen, *Sci. Rep.* **8**, 1 (2018).
  - [7] H. Lamb, *Hydrodynamics* (Cambridge University Press, Cambridge, UK, 1916).
  - [8] M. S. Plesset, *J. Appl. Phys.* **25**, 96 (1954).
  - [9] T. B. Benjamin and M. Strasberg, *J. Acoust. Soc. Am.* **30**, 697 (1958).
  - [10] A. Francescutto and R. Nabergoj, *Acustica* **41**, 215 (1978).
  - [11] R. Nabergoj and A. Francescutto, *J. Phys. Colloques* **40**, C8-306 (1979).
  - [12] M. Versluis, D. E. Goertz, P. Palanchon, I. L. Heitman, S. M. van der Meer, B. Dollet, N. de Jong, and D. Lohse, *Phys. Rev. E* **82**, 026321 (2010).
  - [13] M. Guédra, S. Cleve, C. Mauger, P. Blanc-Benon, and C. Inserra, *Phys. Rev. E* **96**, 063104 (2017).
  - [14] S. Cleve, M. Guédra, C. Inserra, C. Mauger, and P. Blanc-Benon, *Phys. Rev. E* **98**, 033115 (2018).
  - [15] A. van Wamel, K. Kooiman, M. Hartevelde, M. Emmer, F. J. ten Cate, M. Versluis, and N. de Jong, *J. Control. Rel.* **112**, 149 (2006).
  - [16] H. J. Vos, B. Dollet, M. Versluis, and N. de Jong, *Ultrasound Med. Biol.* **37**, 935 (2011).
  - [17] F. Prabowo and C.-D. Ohl, *Ultrason. Sonochem.* **18**, 431 (2011).
  - [18] P. Marmottant, M. Versluis, N. de Jong, S. Hilgenfeldt, and D. Lohse, *Exp. Fluids* **41**, 147 (2006).

- [19] O. A. Abramova, I. Sh. Akhatov, N. A. Gumerov, Yu.A. Pityuk, and S. P. Sametov, [Fluid Dyn.](#) **53**, 337 (2018).
- [20] F. Mekki-Berrada, P. Thibault, and P. Marmottant, [Phys. Fluids](#) **28**, 032004 (2016).
- [21] V. Garbin, D. Cojoc, E. Ferrari, E. Di Fabrizio, M. L. J. Overvelde, S. M. van der Meer, N. de Jong, D. Lohse, and M. Versluis, [Appl. Phys. Lett.](#) **90**, 114103 (2007).
- [22] B. Dollet, S. M. van der Meer, V. Garbin, N. de Jong, D. Lohse, and M. Versluis, [Ultrasound Med. Biol.](#) **34**, 1465 (2008).
- [23] A. O. Maksimov, [J. Sound Vib.](#) **283**, 915 (2005).
- [24] S. Shklyaev and A. V. Straube, [Phys. Fluids](#) **20**, 052102 (2008).
- [25] P. R. Birkin, Y. E. Watson, and T. G. Leighton, [Chem. Commun.](#) **24**, 2650 (2001).
- [26] S. Courty, G. Lagubeau, and T. Tixier, [Phys. Rev. E](#) **73**, 045301(R) (2006).
- [27] C. T. Chang, J. B. Bostwick, P. H. Steen, and S. Daniel, [Phys. Rev. E](#) **88**, 023015 (2013).
- [28] A. O. Maksimov and T. G. Leighton, [Proc. R. Soc.](#) **468**, 57 (2012).
- [29] M. Guédra, C. Inserra, C. Mauger, and B. Gilles, [Phys. Rev. E](#) **94**, 053115 (2016).
- [30] J. B. Bostwick and P. H. Steen, [J. Fluid Mech.](#) **760**, 5 (2014).
- [31] P. V. R. Suryanarayana and Y. Bayazitoglu, [Phys. Fluids A](#) **3**, 967 (1991).
- [32] C. T. Chang, J. B. Bostwick, S. Daniel, and P. H. Steen, [J. Fluid Mech.](#) **768**, 442 (2015).
- [33] A. Prosperetti, [Phys. Fluids](#) **24**, 032109 (2012).
- [34] P. R. Birkin, D. G. Offen, C. J. B. Vian, T. G. Leighton, and A. O. Maksimov, [J. Acoust. Soc. Am.](#) **130**, 3297 (2011).